

# Galvanic Corrosion Underlies Coulombic Efficiency Differences in High-Performing Lithium Metal Battery Electrolytes

Solomon T. Oyakhire<sup>1,2†</sup>, Sang Cheol Kim<sup>3†</sup>, Wenbo Zhang<sup>3†</sup>, Sanzeeda Baig Shuchi<sup>1†</sup>, Yi Cui<sup>3,4,5\*</sup>, Stacey F. Bent<sup>1,4\*</sup>

1 Department of Chemical Engineering, Stanford University, Stanford, CA 94305, USA.

2 Department of Materials Science and Engineering, University of California, Berkeley, CA 94720, USA

3 Department of Materials Science and Engineering, Stanford University, Stanford, CA 94305, USA.

4 Department of Energy Science and Engineering, Stanford University, Stanford, CA 94305, USA.

5 Stanford Institute for Materials and Energy Sciences, SLAC National Accelerator Laboratory, 2575 Sand Hill Road, Menlo Park, CA 94025, USA.

† equal contributions.

## Abstract

Current guidelines for electrolyte engineering in lithium metal batteries are based on design metrics such as lithium morphology, electrolyte transport properties, solid electrolyte interphase (SEI) characteristics, and lithium-electrolyte reactivity. In our work, we show that those design metrics fail to account for performance differences in new high-performing electrolytes whereas galvanic corrosion does. This insight regarding the importance of galvanic corrosion is enabled by the combination of machine learning with rigorous experimental characterization. First, we partition our electrolyte data into low and high Coulombic efficiency (CE) segments to obtain an interpretable machine learning model which informs the design of high-performing (high CE) electrolytes. We design new model-guided, high-performing electrolytes and use spectroscopy and electroanalytical methods to demonstrate the weak correlation between common design metrics and performance in the high-performing electrolytes. Our work results in the design of a high-performing electrolyte with a Coulombic efficiency (CE) of 99.6%, a new understanding that common performance indicators are not sufficient for informing the development of high-performing electrolytes, and the identification of galvanic corrosion as an important performance driver in high-performing electrolytes.

## Introduction

The commercial deployment of lithium metal batteries could revolutionize energy storage.<sup>1</sup> Yet, the reactivity of lithium, coupled with resulting lithium losses, pose a formidable challenge in achieving the battery cycling efficiencies required for commercial viability.<sup>1,2</sup> One promising method for controlling the reactivity of lithium metal is the design of battery electrolytes.<sup>3</sup> Beyond their role as conduits for ion transport between battery electrodes, electrolytes interface with lithium metal, offering opportunities to stabilize the surface of lithium, prevent lithium loss, and improve battery cycling efficiency. As a result, many research efforts in lithium metal batteries have been focused on electrolyte design.<sup>4-8</sup>

Most efforts in electrolyte design are focused on the molecular engineering of liquid electrolytes. In lithium metal batteries, a liquid electrolyte comprises solvents that coordinate with (solvate) lithium salts and, in some cases, additives as well. As such, the design of liquid electrolytes for improved battery cycling efficiency is achieved by modifying solvents,<sup>9,10</sup> salts,<sup>11,12</sup> and additives.<sup>13–15</sup> By changing the chemistry and concentration of liquid electrolyte components, it is possible to modify their thermodynamic stability, reactivity with lithium, and the nature of the interface which forms after they react with lithium. These properties of liquid electrolytes impact the quantity of lithium that is available during battery discharge, and this quantity is described by an important parameter known as Coulombic efficiency (CE). An ideal lithium metal battery would have a CE of 100%, concomitant with zero loss of lithium in each battery cycle. Due to clever electrolyte design, research on lithium metal batteries over the past few decades has achieved more than 10% increase in CE, with state-of-the-art electrolytes displaying CEs of about 99.5%.<sup>16</sup> However, electrolyte CEs have reached an apparent plateau in recent years. While 99.5% CE is an impressive feat, lithium metal batteries need to achieve CEs greater than 99.9% to become commercially compelling.

It is challenging to design electrolytes that substantially exceed 99.5% CE because of our limited understanding of what drives CE in high CE (defined here as >98%) electrolytes. Current electrolyte design strategies draw insights from measurements and characterizations of properties that discern electrolyte differences across a large CE range (80% – 99.5%). Examples of such properties are lithium morphology,<sup>17–20</sup> electrolyte transport properties,<sup>8,21</sup> and solid electrolyte interphase (SEI) characteristics.<sup>22–24</sup> However, these global insights obtained from comparisons between low and high CE electrolytes can fail to inform localized improvements in high CE electrolytes. For instance, lithium morphology is often used as a CE indicator on the basis that low and high CE electrolytes yield contrasting lithium contact area morphologies. Given that lithium contact area could indicate the extent of lithium-electrolyte reactions (high contact area indicates increased reactions), morphology measurements have evolved into an integral tool for lithium metal battery characterization and CE inference. Similarly, the chemistry of the solid electrolyte interphase (SEI) which forms after lithium-electrolyte reactions is also commonly used as an indicator for CE, with low CE electrolytes promoting the formation of SEIs that are rich in solvent-containing species. These solvent-rich SEIs are associated with low CEs in batteries because of their high likelihood of dissolution, high porosity, uptake of solvents (swelling), and susceptibility to electron transport.<sup>25,26</sup> Even though battery properties like lithium morphology and SEI chemistry offer insights into CE differences between low and high CE electrolytes, it is unclear if they are relevant for informing improvements within high CE electrolytes. To design electrolytes that operate with CEs that exceed 99.9%, it is important to thoroughly understand the relevant performance drivers in high CE electrolytes.

In our work, we employ a hybrid approach encompassing data science techniques and a suite of characterization measurements to identify galvanic corrosion as an important, and previously overlooked, driver of performance in high CE electrolytes. Our methodology unfolds in several steps. First, we use a data science workflow bolstered by interpretable machine learning algorithms to identify drivers of performance (electrolyte features such as low solvent oxygen content and high fluorine content) in 93 high CE electrolytes. Next, we design new electrolytes with high CE based on the drivers (key electrolyte features) identified as essential for high performance. In these new high CE electrolytes, we discover discrepancies between predicted and measured CE. These discrepancies suggest that the commonly used drivers of performance which form the basis of our CE predictions

do not account for performance differences in our set of high CE electrolytes. Using a comprehensive suite of measurements, we provide molecular insights into the differences between measured and predicted CE. We reveal that common characterization metrics such as lithium-ion transport, lithium-electrolyte reactivity, lithium morphology, and SEI chemistry do not fully account for performance differences in our high CE electrolytes. Instead, galvanic corrosion explains the performance variations in our series of high CE electrolytes, with CE correlating negatively with increased galvanic corrosion rates. This work provides a crucial insight that guides the lithium metal research community towards the design of electrolytes with CEs that exceed 99.9%.

## Results and Discussion

### *Machine Learning on Segmented CE Data*

To develop and test quantitative relationships between electrolyte properties and CE, we adopted the machine learning workflow shown in Figure 1c. This workflow expands upon the one we reported in our recent work,<sup>27</sup> and that developed by others.<sup>28</sup> First, we selected features that encode electrolyte properties which influence CE in lithium metal batteries (Figure 1a; refer to table 1 for full list and descriptions of features ). Simple electrolyte features were extracted from the elemental constituents of electrolytes and these features encode for physical properties of the electrolytes, reaction products of electrolyte decomposition, and thermodynamic properties of electrolyte mixtures (Figure 1a). This process of feature selection is crucial because physical properties of the electrolyte influence lithium-ion transport, reaction products influence the quality of the SEI, and thermodynamic properties influence the morphology of lithium metal, all of which impact CE. A full descriptive list of these features is presented in table 1.

**Table 1: Complete list of electrolyte features used for machine learning.**

| Feature              | Abbreviation | Description  |
|----------------------|--------------|--|
| Oxygen Ratio         | 0%           | Molar fraction of oxygen in entire electrolyte volume.             |
| Solvent Oxygen Ratio | s0           | Molar fraction of oxygen in solvents in entire electrolyte volume. |
| Anion Oxygen Ratio   | a0           | Molar fraction of oxygen in anion in entire electrolyte volume.    |
| Carbon Ratio         | C%           | Molar fraction of carbon in entire electrolyte volume.             |
| Solvent Carbon Ratio | sC           | Molar fraction of carbon in solvents in entire electrolyte volume. |

|                         |      |  |
|-------------------------|------|--|
| Anion Carbon Ratio      | aC   | Molar fraction of carbon in anion in entire electrolyte volume.                                    |
| Fluorine Ratio          | F%   | Molar fraction of fluorine in entire electrolyte volume.   |
| Solvent Fluorine Ratio  | sF   | Molar fraction of fluorine in solvents in entire electrolyte volume.                               |
| Anion Fluorine Ratio    | aF   | Molar fraction of fluorine in anion in entire electrolyte volume.                                  |
| Fluorine/Oxygen Ratio   | F/O  | Molar ratio of fluorine to oxygen  |
| Fluorine/Carbon Ratio   | F/C  | Molar ratio of fluorine to carbon  |
| Oxygen/Carbon Ratio     | O/C  | Molar ratio of oxygen to carbon  |
| Inorganic/Organic Ratio | InOr | Molar ratio of elements excluding carbon, hydrogen, and lithium (inorganics) to carbon (organics). |

In addition to selecting features which encode for CE predictive power, we segmented our data set of 189 unique electrolytes into low-performance and high-performance (defined here as CE >98%) segments (Figure 1b). This segmentation is necessary for identifying performance drivers that are unique to low CE and high CE electrolytes and enabling segment specific improvements in CE. In addition, we selected 98% as the threshold between low and high CE electrolytes because it results in a sufficient and similar number of data points across both classes (>90), providing a fair basis for comparing statistical insights. Finally, we defined efficiency (the predicted variable) as a logarithmic transformation of CE to increase the variability of CE and improve the likelihood that our algorithms capture the relationships between CE and the electrolyte features (Figure 1b, left axis; equation 1).

$$\text{Efficiency} = -\log(1 - \text{CE}) \quad (1)$$

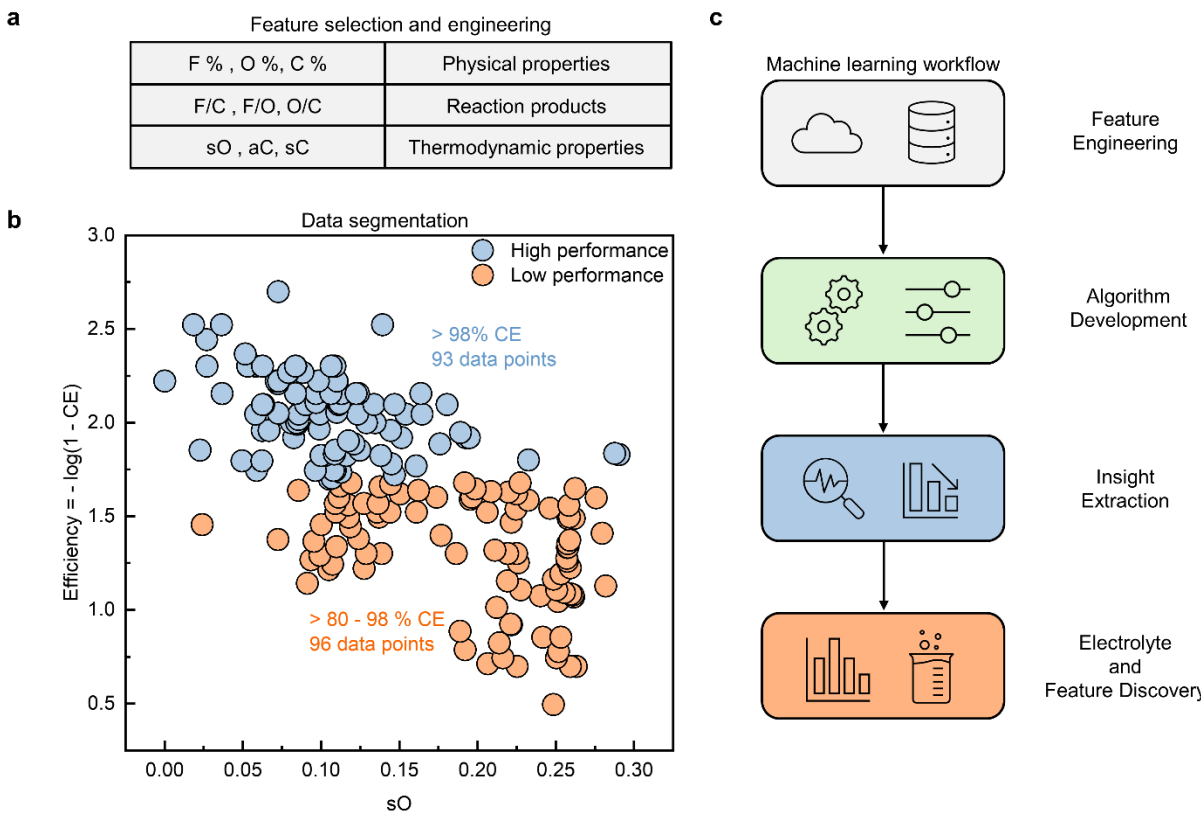


**Figure 1:** Machine learning process for understanding performance drivers in liquid electrolytes.

- Electrolyte properties encoded in machine learning features. F%, O%, and C% represent the molar fraction of F, O, and C in the entire electrolyte volume, respectively. F/C, F/O, and O/C represent the ratios of molar fractions of corresponding elements. sO, aC, and sC represent the molar fraction of oxygen in solvents, molar fraction of carbon in anions, and molar fraction of carbon in solvents in the entire electrolyte volume. The full description of abbreviated features is presented in table 1.
- Efficiency of electrolytes plotted against sO (molar fraction of oxygen in solvents in the entire electrolyte volume).
- Overall machine learning workflow for electrolyte and feature discovery.

### Model Selection and Insight Extraction

We used machine learning models to identify the most important features for predicting electrolyte efficiency. Each electrolyte group contains approximately 95 data points and 13 features, so to avoid overfitting our data to the 13 features, we applied feature pruning methods.<sup>27,29</sup> First, we used forward stepwise selection to identify the best 1-feature - 7-feature linear models that correlate strongly with efficiency (Supplementary Figure 1). Because the forward stepwise selection models were trained and tested on the same data, they run the risk of poorly generalizing to other data sets, even though the residual sum of squares (RSS) reduces as the number of features increases (Supplementary Figure 2). To address this issue, we calculated mean cross validation (CV) errors for

the low CE and high CE electrolytes as a metric of model generalizability to unseen data (Figures 2a-2b). To augment the mean CV calculations, we used the probably approximately correct (PAC) theory to estimate a model generalizability boundary shown as dashed lines (Figures 2a-2b and supplementary note).<sup>30</sup> The PAC equation used to calculate the boundary is shown in equation 2

$$\varepsilon \leq \sqrt{\frac{(m+1) \ln\left(\frac{2n}{m+1} + 1\right) + \ln\left(\frac{4}{\delta}\right)}{n}} \quad (2)$$

where  $\varepsilon$  represents the acceptable difference between test and validation errors,  $m$  represents the number of features,  $n$  represents the number of observations, and  $1-\delta$  represents the level of confidence in the estimate of  $\varepsilon$  for given  $m$  and  $n$ . The PAC boundaries presented in figures 2a-2b were obtained for an  $\varepsilon$  of 50% and a confidence level of 95%.

By combining mean CV with PAC, we observed that predictive errors generally reduced as the number of features increased until a critical point just before the PAC boundary (Figures 2a-2b). This observation indicates that the four-feature models provide the highest degree of generalizability while simultaneously minimizing the risk of overfitting. It is crucial to point out here that the four-feature models are different in the low CE and high CE electrolytes, with each model governed by a distinct equation (equations 3 and 4).

$$Efficiency = -0.412 \frac{F}{O} - 1.89sO + 4.10sF - 3.70C + 2.63 \quad (3)$$

$$Efficiency = 0.03 \frac{F}{O} - 1.20sO + 0.75sC - 0.63aF + 1.98 \quad (4)$$

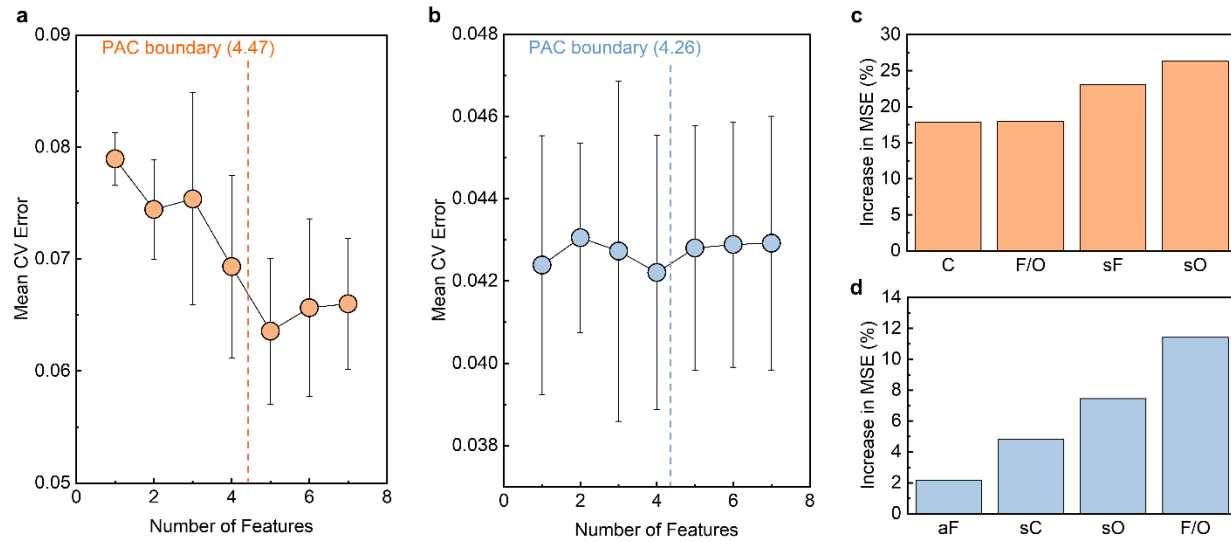


**Figure 2:** Model selection and feature importance ranking for low and high-performing electrolytes.

Cross validation errors and PAC boundary for (a) low-performing electrolytes and (b) high-performing electrolytes. Error bars indicate standard deviation for cross validation errors calculated using 10 different data partitions.

Percentage increase in mean squared errors (MSE) in the absence of each feature in the four-feature models for (c) low-performing electrolytes and (d) high-performing electrolytes.

The difference in optimal models in both electrolyte classes suggests that different features drive efficiency in each class. Specifically, sO and F/O are common to both electrolyte performance classes, suggesting that efficiency improvements in both low CE and high CE electrolytes have benefitted from an increase in solvation free energy of lithium ions (reduction in sO) and changes in electrolyte fluorine content (changes in F/O). However, a correlation between increasing CE and a decrease in C is unique to the low CE electrolytes perhaps because successful design strategies in the low CE regime focused on reducing overall carbon content of electrolytes. Meanwhile, increasing sC correlates strongly with increasing CE only in the high CE electrolytes, suggesting that the modulation of carbon content has become focused on solvents in high CE electrolytes. These correlations represent unifying insights across seemingly different electrolyte chemistries that are present in our data set. It is noteworthy that when the data is aggregated, the model obtained for all 189 electrolytes differs from those obtained in the individual electrolyte CE categories (Equation 5). The unique models in each CE class indicate that global trends and insights may not be useful in different CE classes, so local insights are invaluable for advancing electrolyte development in the high CE segment.

$$\text{Efficiency} = 1.2128sF - 3.52sO + 2.33aO - 9.65aC + 2.065 \quad (5)$$

To understand the importance of each feature in the four-feature models identified in Figures 2a-2b, we built random forest models for predicting efficiency from those features.<sup>29</sup> By calculating the importance of each feature in 200 random forest trees, we ranked each feature in the four-feature models (Figures 2c-2d). These rankings were determined based on the percentage increase in mean squared error when each feature was excluded from the random forest prediction. As shown in Figures 2c and 2d, sO and sF are the most important drivers of performance variation in the low CE range, closely followed by F/O and C while F/O and sO are the most important drivers of performance variation in the high CE range. These rankings are useful because they could be used to inform the experimental design of new high CE electrolytes.

### ***Model-Informed High-Performance Electrolyte Design and Testing***

The design of new high CE electrolytes is important for the realization of lithium metal batteries, yet this process is mostly informed by trial-and-error. Our results in Figure 2d indicate that high CE electrolytes can be discovered by systematically varying sO and F/O. Specifically, low sO and high F/O can serve as the basis for designing high-performing electrolytes. As such, the boundary of our experimental search for new electrolytes was defined based on the numerical ranges of sO and F/O in our high CE electrolyte data. Using this boundary, we selected five ether solvents and paired them with 1 M LiFSI salt to make new electrolytes (Figure 3a). In this selection of new electrolytes which satisfy the algorithm-informed requirements for high CE, we also varied some important molecular properties of the solvents to capture molecular characteristics that could be missed by our simple algorithm. Specifically, among diethyl ether (DEE), dipropyl ether (DPE), and dibutyl ether (DBE), we increased the chain length of hydrocarbons that surround the solvating oxygen atom. Also, between ethyl butyl ether (EBE), dipropyl ether (DPE), and diisopropyl ether (DiPE), we varied the symmetry

of the hydrocarbons that surround the solvating oxygen atom. These variations in chain length and symmetry could affect the solvation strength of oxygen (equivalently the solvation energy of lithium ions) and modify lithium transport, and as such, offer insights into CE that are not captured by the simple design rules offered by our model.

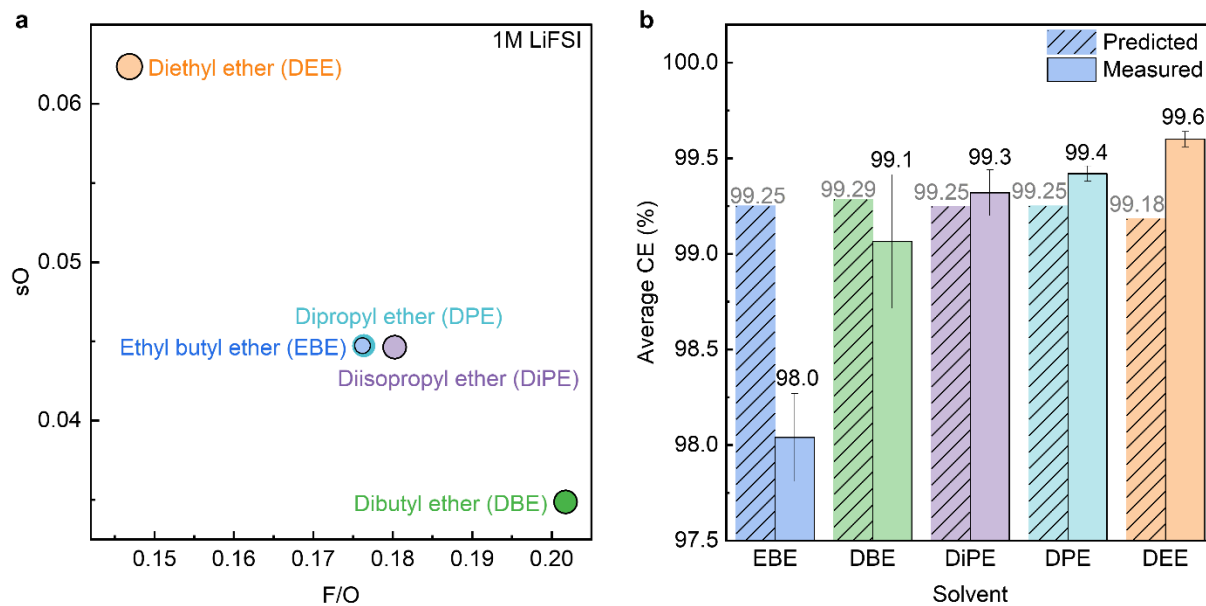


**Figure 3:** Identification and testing of ML-informed high-performance electrolytes.

- sO and F/O values for the new solvents selected in our study.
- Predicted and measured average CE values for our high-performance electrolytes. Error bar in measured CE represents the standard deviation calculated using three cells.

To assess the efficacy of the machine learning model, we compared the predicted and measured values of CE (Figure 3b). Because most electrolytes used for training the ML model were tested using the Aurbach CE method, we tested our new electrolytes using the Aurbach method to provide a fair basis for comparing predictions and measurements. As shown in Figure 3b, the predicted CE differs from the measured CE for some of the tested electrolytes. Due to the narrow range of sO and F/O used for designing the new electrolytes, their model-predicted CEs lie very close to each other, ranging from 99.18% to 99.29%. However, the measured CE values range from 98% to 99.6%, showing that there is some discrepancy between the model and experiments. The mismatch between prediction and measurements is more obvious when we focus on the electrolytes made from the EBE solvent and the DEE solvent; While the model predicts DEE to have the lowest CE, its measured CE is the highest, and while the model predicts that EBE will have a high CE, its measured CE is the lowest. Even though all the measured CEs lie within the high-performance range (>98% CE) predicted by the model, the differences between measured and predicted CEs still need to be rationalized. Specifically, it is important to understand why the performance indicators encoded in the machine learning model fail to capture CE differences in our high-performing electrolytes.

### ***Electrolyte Characterization and Model Descriptor Analysis***

We used a suite of characterization tools to measure common indicators of performance in lithium metal batteries and correlate them with CE in our new high-performing electrolytes. First, we used scanning electron microscopy to visualize the morphology (growth structure) of lithium and observe that lithium forms compact morphologies in all the electrolytes (Figure 4a, Supplementary Figure 3). These compact morphologies indicate a low contact area between lithium and the electrolyte which could result in reduced lithium-electrolyte reactions during battery cycling. The similarity in lithium morphologies formed on all substrates suggests that their CE differences cannot be attributed to lithium morphology. Next, we investigated the steady-state potential for lithium stripping in all the electrolytes (Figure 4b). The stripping potential for lithium is the overpotential needed to oxidize lithium and transport it to the counter electrode during discharge. Our results in Figure 4b indicate that there is no clear trend between steady state stripping potential and stripping time before the cutoff potential (longer stripping time indicates higher CE). Even though EBE has one of the lowest stripping overpotentials, it does not display a high CE, suggesting that the differences in CE observed between these electrolytes is likely not due to charge-transfer kinetics or lithium-ion transport differences. Another important property is ion transport, where we observe that the electrolytes have varying ionic conductivity, from 0.7 mS/cm to 4.1 mS/cm (Figure 4d). We also observe that ionic conductivity does not correlate with CE, so it does not fully account for the observed differences in CE among all 5 electrolytes (Figure 4d and additional Nyquist plots shown in Supplementary Figure 4). Interestingly, ionic conductivity correlates negatively and strongly with stripping overpotential; electrolytes with low stripping overpotential have high ionic conductivity and vice versa (Figure 4d). This indicates that the differences in stripping overpotential observed in Figure 4b could be partly attributed to differences in ionic conductivity in those electrolytes.

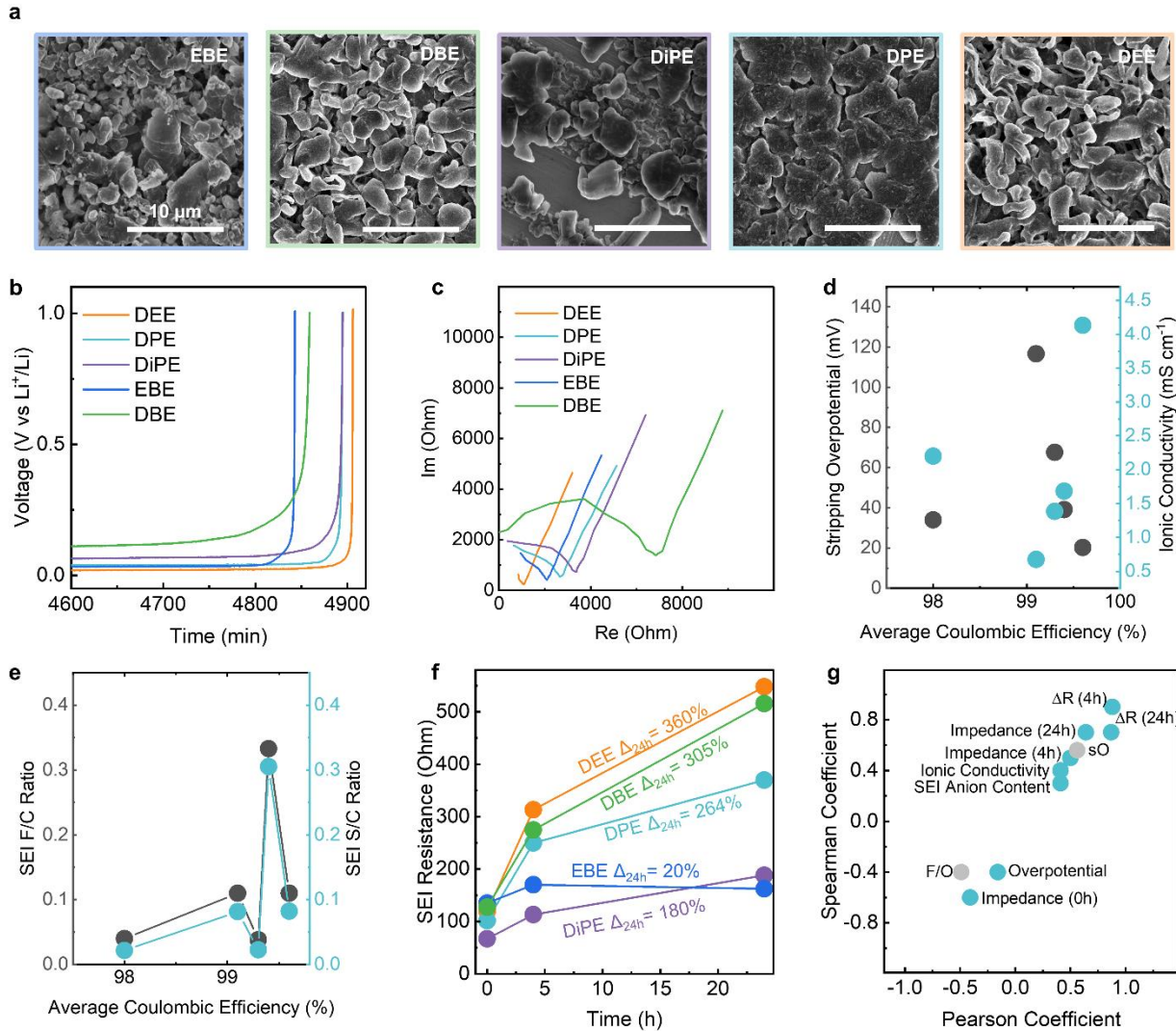


**Figure 4:** Relationship between common performance indicators and Coulombic Efficiency in high-performance electrolytes.

- Morphology of  $0.5 \text{ mAh}$  of lithium grown at  $0.5 \text{ mA cm}^{-2}$  in our high-performance electrolytes
- Lithium stripping overpotential in our high-performance electrolytes at the end of Aurbach tests carried out at  $0.5 \text{ mA cm}^{-2}$ .
- Nyquist plots of lithium-ion conductivity measurements on our high-performance electrolytes.
- Lithium stripping overpotential and ionic conductivity plotted as a function of electrolyte CE.
- Atomic ratios of SEI components formed on  $0.5 \text{ mAh}$  of lithium grown at  $0.5 \text{ mA cm}^{-2}$  in our high-performance electrolytes.
- Evolution of SEI resistance over time in our high-performance electrolytes tested using  $\text{Li}|\text{Li}$  cells.
- Spearman and Pearson coefficients of common performance indicators in relation to CE for our high-performance electrolytes, where  $\Delta R(t)$  represents the ratio of SEI impedance measured at time  $t$  relative to SEI impedance measured at time  $t = 0\text{h}$ . Teal markers represent

measured performance indicators and grey markers represent calculated machine learning design parameters.

Another common performance indicator for lithium metal batteries is SEI chemistry. In particular, SEIs predominantly made up of anions (typically termed anion-rich) are considered beneficial for lithium metal because they reduce the infiltration of reactive solvents towards the surface of lithium, and they reduce electron transport from lithium to the electrolyte.<sup>25,26</sup> Using X-ray photoelectron spectroscopy (XPS), we measured the SEI chemistry of our high-performing electrolytes.<sup>31</sup> We quantified the F/C and S/C ratios because they indicate the anion prevalence of species in the SEI as F and S are unique to the anions while C is unique to the solvents (Figure 4e). As shown in Figure 4e, there is no clear correlation between anion prevalence in the SEI and Coulombic efficiency, indicating that the differences in performance of our electrolytes cannot be attributed only to SEI chemistry.

Lithium-electrolyte reactivity is also another performance indicator used in lithium metal batteries.<sup>32,33</sup> High-performing electrolytes are associated with low lithium-electrolyte reactivity. To quantify the reactivity of our high-performing electrolytes, we used electrochemical impedance spectroscopy to measure the change in SEI resistance when the electrolytes are sandwiched between two uncycled lithium electrodes (Figure 4f). Surprisingly, the worst performing electrolyte (EBE) displays one of the lowest initial SEI resistances ( $t = 0\text{h}$ ) (Figure 4f). This low CE and low SEI resistance observation is counter-intuitive because the initial SEI resistance (at  $t=0\text{h}$ ) is often negatively correlated with CE. Lower SEI resistance promotes lower overpotentials and a reduced likelihood of forming lithium-ion concentration gradients, both of which are associated with improved battery performance.<sup>34,35</sup> In addition, the best performing electrolyte (DEE) displays the highest increase in SEI resistance over a 24-hour period ( $\Delta_{24\text{h}}$ ) (Figure 4f). This high increase in SEI resistance is indicative of high reactivity between lithium and the high-performing DEE electrolyte, suggesting that lithium-electrolyte reactivity rate is not the sole determinant of battery performance. It is also noteworthy that the low increase in SEI resistance observed in the poor-performing EBE electrolyte may not be directly indicative of low Li-electrolyte reactivity, but rather reflective of high SEI dissolution rates.

With the results from various characterization techniques failing to identify a correlation, we quantified the correlation between CE and the performance indicators using Pearson and Spearman correlation coefficients. The Pearson coefficient quantifies the correlation between variables while assuming a linear relationship between them while the Spearman coefficient quantifies correlation without making linearity assumptions.<sup>36</sup> Both correlation measures return values that lie between -1 and 1, with -1 indicating perfect negative correlation and 1 indicating perfect positive correlation. Using both coefficients adds robustness to our correlation analysis. The correlation coefficients for the performance indicators measured in Figure 4 are represented by the teal markers in Figure 4g while those for the machine learning design parameters ( $s_0$  and  $F/O$ ) are shown in the grey markers. Most of the indicators and parameters displayed in Figure 4g display weak negative and positive correlations, as their coefficients lie between -0.6 and 0.6. This weak correlation suggests that most of the parameters encoded in the algorithm and measured experimentally do not account for the differences in CE observed in our high-performing electrolytes.

A few other parameters, however, reflect some surprising and counterintuitive strong correlations. These parameters, such as the increase in SEI resistance ( $\Delta R$ ) after 4 hours and 24 hours and the absolute SEI resistance after 24 hours, correlate positively and strongly (coefficient  $>0.6$ ) with CE. This finding is counterintuitive because SEI resistance increase is indicative of SEI growth driven by

lithium-electrolyte reactions. Lithium-electrolyte reactions are tantamount to lithium loss which leads to low CE, so the strong positive correlations between CE and SEI resistance increase (increasing lithium loss) are unexpected. This counterintuitive trend indicates that electrolyte reactivity during battery cycling is not fully captured by Li|Li aging experiments. There are a few possible reasons for this. First, some of the products of Li-electrolyte reactions may have high dissolution rates, making the timescale of impedance measurements insufficient for identifying the correct quantity of SEI species formed from Li-electrolyte reactions. Second, it is also possible that during continuous battery cycling, the SEI species formed at Li deposition potentials provide different passivation than the SEI formed on native Li which was used for our aging experiments. These collectively show that Li|Li aging measurements do not fully reflect lithium stability in battery cycling. Due to the weak and misleading correlations between common performance indicators and CE in high-performing electrolytes, it is important to carefully investigate other performance indicators.

### ***Galvanic Corrosion as an Indicator of CE in High-Performing Electrolytes***

To identify other useful performance indicators, it is important to consider why common indicators fail to account for CE differences in high-performing electrolytes. For electrolytes to be high performing (CE >98%), they probably have certain rudimentary properties such as the formation of low surface area lithium, the formation of a passivating SEI, and the promotion of low overpotential during cycling. However, because all high-performing electrolytes likely satisfy these rudimentary criteria, it is difficult to use those criteria in differentiating them. In identifying alternate indicators of CE in high performing electrolytes, it is important to look at properties that contribute to small amounts of performance losses. One property that could be useful for understanding performance differences in high CE electrolytes is galvanic corrosion.<sup>37,38</sup> Electrolytes are not commonly designed to minimize galvanic corrosion because it does not drive substantial amounts of lithium loss. However, galvanic corrosion could be a valuable differentiator in high-performance regimes where lithium loss due to other significant factors is subdued.

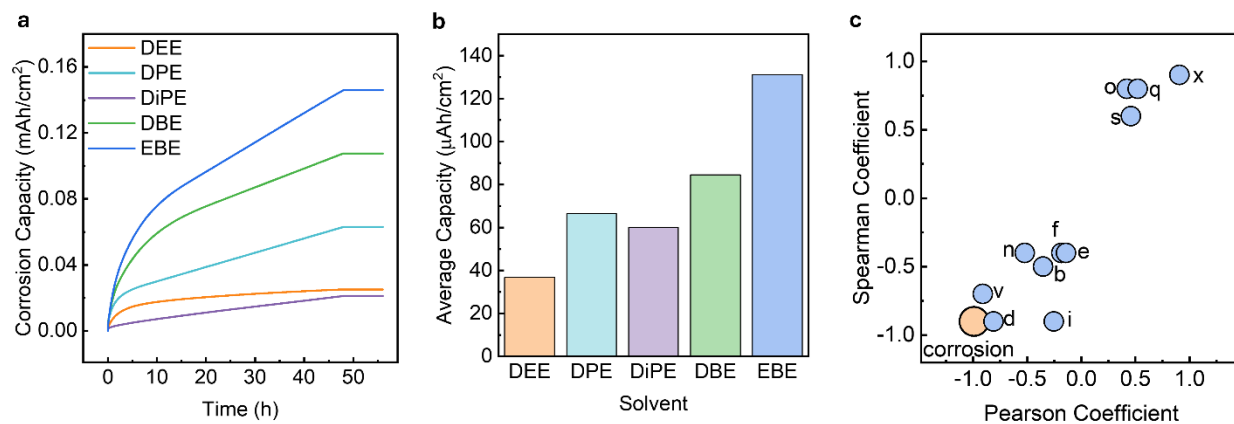


**Figure 5:** Relationship between corrosion and Coulombic efficiency in high-performance electrolytes.

- Corrosion capacity over time in high-performance electrolytes.
- Average corrosion capacity for high-performance electrolytes calculated using two cells per electrolyte.

c. Correlation coefficients for corrosion and some derivative features in relation to CE for high-performance electrolytes.

To quantify the extent of galvanic corrosion in our five high-performing electrolytes, we performed voltage step measurements from open-circuit voltage (OCV) to 15 mV vs Li/Li<sup>+</sup> and measured the corrosion current as the cells were held at 15 mV for 48 hours. By integrating the corrosion current over time, we obtained the corrosion capacity, which is plotted as a function of time in Figure 5a. There is a negative correlation between corrosion capacity and the performance of our electrolytes, with DEE showing the lowest average corrosion capacity and EBE showing the highest corrosion capacity (Figure 5b). These measurements suggest that the driving force for lithium loss due to electron transfer to copper at the lithium-copper interface (galvanic corrosion) explains the differences in CE observed in our high-performing electrolytes. Specifically, the lower tier, high-performing electrolytes such as EBE and DBE have a higher driving force for the corrosion reaction than the higher tier, high-performing electrolytes such as DEE and DPE. The Pearson and Spearman coefficients for the correlation between CE and this corrosion capacity are -1 and -0.9, respectively, indicating a strong negative correlation between CE and corrosion (Figure 5c). This corrosion parameter provides a stronger correlation with and a more intuitive explanation of the CE differences in our high-performing electrolytes than the parameters displayed in Figure 4g. To further demonstrate the strength of the corrosion parameter, we compared its correlation coefficient with those of ratios and products of the parameters presented in Figure 4g (refer to Supplementary table 1 for list of parameters). These ratios and products likely capture correlations that are not obvious in individual parameters. Yet, we observe that the corrosion parameter is more strongly correlated with CE than the ratios and products (Figure 5c), showing that galvanic corrosion is an important driver of CE in high-performing electrolytes.

## Conclusions

In our work, we have demonstrated that galvanic corrosion explains differences in CE of high-performing lithium metal battery electrolytes better than commonly used performance indicators. By using machine learning models which contained common performance indicators, we extracted electrolyte design insights that informed the synthesis of new high-performing electrolytes. These new high-performing electrolytes have CEs that range from 98% to 99.6%, and while the machine learning models predicted that they would be high-performing (>98 % CE), there were discrepancies between the measured and predicted CEs. This discrepancy suggested that the common performance indicators encoded within the machine learning models did not account for CE differences in high-performing electrolytes. Using spectroscopy and electroanalytical methods, we measured the common performance indicators such as lithium morphology, lithium-ion conductivity, SEI chemistry, and lithium-electrolyte reactivity. Using correlation coefficients, we demonstrated only weak correlations between the CE of high-performing electrolytes and common performance indicators. Subsequently, we presented galvanic corrosion as a crucial driver of CE for these high-performing electrolytes, revealing the importance of new metrics in the design of high CE electrolytes.

## Methods

### Data Acquisition and Processing

Coulombic efficiency data was extracted from literature reports in which Li|Cu cells were used for battery testing and current densities close to 0.5mA/cm<sup>2</sup> were used for cycling. The formula of each reported electrolyte was used for calculating elemental composition. Machine learning features were subsequently obtained from electrolyte composition as described in our previous paper.<sup>27</sup>

### Machine Learning Model Development

In this work, we carried out model fitting (estimating the coefficient values) and model selection (establishing the model structure). We employed forward stepwise selection to carry out model fitting and selection.

A linear model of the form:

$$\hat{y}_i = \hat{\mathbf{w}}^T \mathbf{x}_i$$

was proposed, where  $\hat{y}_i$  represents the predicted LCE of a given electrolyte i,  $\mathbf{x}_i$  represents a p-dimensional feature vector for a given electrolyte and  $\hat{\mathbf{w}}^T$  represents the p-dimensional coefficient vector. To perform forward stepwise selection, we started with a model with zero features and subsequently included features one at a time based on selections which impacted the highest reductions in the residual sum of squares (RSS).

The formula for RSS is:

$$RSS = \sum_{i=1}^n (y_i - \hat{y}_i)^2$$

where  $y_i$  is the n-dimensional vector for all experimentally observed LCEs and n represents the number of observations (unique data points).

The generalizability of the models selected using forward were tested against both data segments (low CE and high CE data) using four-fold cross validation. The best performing models were selected based on PAC errors and CV error estimates ( $CV_{(K)}$ ) which were calculated thus:

$$CV_{(K)} = \sum_{k=1}^K \frac{n_k}{n} MSE_k$$

where K is the number of folds in which the data was divided for CV,  $n_k$  is the number of observations in each of the K folds, and  $MSE_k$  is the mean-squared error for the observations in each of the K folds, with the MSE calculated using the following equation:

$$MSE = \frac{1}{n} \sum_{i=1}^n (y_i - \hat{y}_i)^2$$

In summary, we divided our literature data into low and high CE data sets. We selected the most reliable models using forward stepwise selection, then we used those models to inform the design of new high performing electrolytes. All the data processing and prediction were performed in R using the MASS, ISLR, leaps, tree, gbm, and randomForest libraries.

### Coulombic Efficiency Measurement

Electrolytes were prepared and handled in an argon filled glovebox with O<sub>2</sub> concentration < 0.2 ppm and H<sub>2</sub>O concentration < 0.01 ppm. All electrolyte materials were used as received. LiFSI (Fluolyte) was used as the salt and EBE, DBE, DiPE, DPE, and DEE (all from Sigma-Aldrich) were used as solvents. In an argon-filled glovebox, Li | Cu batteries were assembled into type 2032 coin cells. In each coin cell, we used 1 cm<sup>2</sup> (750 µm thick) Li foil (Alfa Aesar), a Cu foil, a separator (Celgard 2325) and 40 µL of electrolyte. A Land Instruments battery tester was used to cycle the coin cells. The cells were tested using the Aurbach method. Specifically, for each cell, using a current density of 0.5 mA cm<sup>-2</sup>, 5 mA h cm<sup>-2</sup> of Li metal was deposited on Cu and stripped (formation cycle). Subsequently, 5 mA h cm<sup>-2</sup> of Li metal was deposited at 0.5 mA cm<sup>-2</sup>, serving as a Li reservoir. Afterwards, 1 mA h cm<sup>-2</sup> of Li was repeatedly stripped and plated at 0.5 mA cm<sup>-2</sup> for 9 cycles. The remaining Li on Cu was then stripped, and the average CE was calculated by dividing the total stripping capacity by the total plating capacity after the formation cycle. In all deposition and stripping steps, the current density was 0.5 mA cm<sup>-2</sup>, and three cells were tested for each electrolyte.

### Electrolyte and Electrode Characterization

Ionic conductivity measurements were carried out using a Swagelok cell which contained symmetric stainless-steel electrodes and no separator. Electrochemical impedance spectroscopy was used to measure the bulk resistance to Li-ion transport in each electrolyte. Resistance was subsequently converted into conductivity using the length and area of the cell.

Scanning electron microscopy (SEM) experiments were performed using an FEI Magellan 400 XHR. X-ray photoelectron spectroscopy (XPS) data were collected on a PHI VersaProbe 1 scanning XPS microprobe with an Al K $\alpha$  source. The SEM and XPS samples were prepared thus: 0.5 mAh of lithium was deposited atop Cu at 0.5 mA cm<sup>-2</sup> in a Li|Cu cell. Cells were disassembled in an argon-filled glove box and lithium samples were cleaned with about 100 µL of the constituent solvents of electrolytes used for lithium deposition. The cleaned Li samples were placed in an airtight and a vacuum transfer vessel, then transferred into the SEM and XPS equipment, respectively.

### Author Contributions

S.T.O: Conceptualization, data engineering and model development, electrochemistry measurements, formal analysis, writing – original draft.

S.C.K: Conceptualization, data engineering and model development, electrochemistry measurements, formal analysis, writing – original draft.

W.Z: Microscopy measurements, electrochemistry measurements, formal analysis, writing – reviewing and editing.

S.B.S: Spectroscopy measurements, electrochemistry measurements, formal analysis, writing – reviewing and editing.

Y.C: Conceptualization, supervision, writing -reviewing and editing.

S.F.B: Conceptualization, supervision, writing -reviewing and editing.

## Acknowledgements

S.T.O acknowledges support from the TomKat Center Fellowship for Translational Research at Stanford University and the Knight-Hennessy scholarship for graduate studies at Stanford University. S.B.S acknowledges support from the Link Foundation Energy Fellowship. Y.C and S.B.S acknowledge support from the Assistant Secretary for Energy Efficiency and Renewable Energy, Vehicle Technologies Office, of the U.S Department of Energy under the Battery Materials Research Program. Y.C acknowledges support from Battery 500 and the CEI consortium. XPS and SEM measurements were performed using the Stanford Nano Shared Facilities, supported by the National Science Foundation under the award ECCS-2026822.

## References

- (1) Liu, J.; Bao, Z.; Cui, Y.; Dufek, E. J.; Goodenough, J. B.; Khalifah, P.; Li, Q.; Liaw, B. Y.; Liu, P.; Manthiram, A.; Meng, Y. S.; Subramanian, V. R.; Toney, M. F.; Viswanathan, V. V.; Whittingham, M. S.; Xiao, J.; Xu, W.; Yang, J.; Yang, X.-Q. Q.; Zhang, J.-G. G. Pathways for Practical High-Energy Long-Cycling Lithium Metal Batteries. *Nat. Energy* **2019**, *4* (3), 180–186. <https://doi.org/10.1038/s41560-019-0338-x>.
- (2) Lin, D.; Liu, Y.; Cui, Y. Reviving the Lithium Metal Anode for High-Energy Batteries. *Nature Nanotechnology*. 2017, pp 194–206. <https://doi.org/10.1038/nnano.2017.16>.
- (3) Wang, H.; Yu, Z.; Kong, X.; Kim, S. C.; Boyle, D. T.; Qin, J.; Bao, Z.; Cui, Y. Liquid Electrolyte: The Nexus of Practical Lithium Metal Batteries. *Joule* **2022**, *6* (3), 588–616. <https://doi.org/10.1016/j.joule.2021.12.018>.
- (4) Yu, Z.; Wang, H.; Kong, X.; Huang, W.; Tsao, Y.; Mackanic, D. G.; Wang, K.; Wang, X.; Huang, W.; Choudhury, S.; Zheng, Y.; Amanchukwu, C. V.; Hung, S. T.; Ma, Y.; Lomeli, E. G.; Qin, J.; Cui, Y.; Bao, Z. Molecular Design for Electrolyte Solvents Enabling Energy-Dense and Long-Cycling Lithium Metal Batteries. *Nat. Energy* **2020**, *5* (7), 526–533. <https://doi.org/10.1038/s41560-020-0634-5>.
- (5) Kim, M. S.; Zhang, Z.; Wang, J.; Oyakhire, S. T.; Kim, S. C.; Yu, Z.; Chen, Y.; Boyle, D. T.; Ye, Y.; Huang, Z.; Zhang, W.; Xu, R.; Sayavong, P.; Bent, S. F.; Qin, J.; Bao, Z.; Cui, Y. Revealing the Multifunctions of Li<sub>3</sub>N in the Suspension Electrolyte for Lithium Metal Batteries. *ACS Nano* **2023**, *17* (3), 3168–3180. <https://doi.org/10.1021/acsnano.2c12470>.
- (6) Zhai, P.; Liu, L.; Gu, X.; Wang, T.; Gong, Y. Interface Engineering for Lithium Metal Anodes in Liquid Electrolyte. *Adv. Energy Mater.* **2020**, *10* (34), 2001257.
- (7) Qian, J.; Henderson, W. A.; Xu, W.; Bhattacharya, P.; Engelhard, M.; Borodin, O.; Zhang, J. G. High Rate and Stable Cycling of Lithium Metal Anode. *Nat. Commun.* **2015**, *6*. <https://doi.org/10.1038/ncomms7362>.

- (8) Amanchukwu, C. V.; Yu, Z.; Kong, X.; Qin, J.; Cui, Y.; Bao, Z. A New Class of Ionically Conducting Fluorinated Ether Electrolytes with High Electrochemical Stability. *J. Am. Chem. Soc.* **2020**, *142* (16), 7393–7403. <https://doi.org/10.1021/JACS.9B11056>.
- (9) Yu, Z.; Rudnicki, P. E.; Zhang, Z.; Huang, Z.; Celik, H.; Oyakhire, S. T.; Chen, Y.; Kong, X.; Kim, S. C.; Xiao, X.; Wang, H.; Zheng, Y.; Kamat, G. A.; Kim, M. S.; Bent, S. F.; Qin, J.; Cui, Y.; Bao, Z. Rational Solvent Molecule Tuning for High-Performance Lithium Metal Battery Electrolytes. *Nat. Energy* **2022**, *7* (1), 94–106. <https://doi.org/10.1038/s41560-021-00962-y>.
- (10) Yu, L.; Chen, S.; Lee, H.; Zhang, L.; Engelhard, M. H.; Li, Q.; Jiao, S.; Liu, J.; Xu, W.; Zhang, J. G. A Localized High-Concentration Electrolyte with Optimized Solvents and Lithium Difluoro(Oxalate)Borate Additive for Stable Lithium Metal Batteries. *ACS Energy Lett.* **2018**, *3* (9), 2059–2067. <https://doi.org/10.1021/acsenergylett.8b00935>.
- (11) Qiao, L.; Oteo, U.; Martinez-Ibañez, M.; Santiago, A.; Cid, R.; Sanchez-Diez, E.; Lobato, E.; Meabe, L.; Armand, M.; Zhang, H. Stable Non-Corrosive Sulfonimide Salt for 4-V-Class Lithium Metal Batteries. *Nat. Mater.* **2022**, *21* (4), 455–462. <https://doi.org/10.1038/s41563-021-01190-1>.
- (12) Jiao, S.; Ren, X.; Cao, R.; Engelhard, M. H.; Liu, Y.; Hu, D.; Mei, D.; Zheng, J.; Zhao, W.; Li, Q.; Liu, N.; Adams, B. D.; Ma, C.; Liu, J.; Zhang, J. G.; Xu, W. Stable Cycling of High-Voltage Lithium Metal Batteries in Ether Electrolytes. *Nat. Energy* **2018**, *3* (9), 739–746. <https://doi.org/10.1038/s41560-018-0199-8>.
- (13) Shi, P.; Zhang, L.; Xiang, H.; Liang, X.; Sun, Y.; Xu, W. Lithium Difluorophosphate as a Dendrite-Suppressing Additive for Lithium Metal Batteries. *ACS Appl. Mater. Interfaces* **2018**, *10* (26), 22201–22209. <https://doi.org/10.1021/acsami.8b05185>.
- (14) Gunnarsdóttir, A. B.; Vema, S.; Menkin, S.; Marbella, L. E.; Grey, C. P. Investigating the Effect of a Fluoroethylene Carbonate Additive on Lithium Deposition and the Solid Electrolyte Interphase in Lithium Metal Batteries Using: In Situ NMR Spectroscopy. *J. Mater. Chem. A* **2020**, *8* (30), 14975–14992. <https://doi.org/10.1039/d0ta05652a>.
- (15) Kasse, R. M.; Geise, N. R.; Sebti, E.; Lim, K.; Takacs, C. J.; Cao, C.; Steinrück, H. G.; Toney, M. F. Combined Effects of Uniform Applied Pressure and Electrolyte Additives in Lithium-Metal Batteries. *ACS Appl. Energy Mater.* **2022**, *5* (7), 8273–8281. <https://doi.org/10.1021/acsaem.2c00806>.
- (16) Hobold, G. M.; Lopez, J.; Guo, R.; Minafra, N.; Banerjee, A.; Shirley Meng, Y.; Shao-Horn, Y.; Gallant, B. M. Moving beyond 99.9% Coulombic Efficiency for Lithium Anodes in Liquid Electrolytes. *Nat. Energy* **2021**, *6* (10), 951–960. <https://doi.org/10.1038/s41560-021-00910-w>.
- (17) Oyakhire, S. T.; Zhang, W.; Shin, A.; Xu, R.; Boyle, D. T.; Yu, Z.; Ye, Y.; Yang, Y.; Raiford, J. A.; Huang, W.; Schneider, J. R.; Cui, Y.; Bent, S. F. Electrical Resistance of the Current Collector Controls Lithium Morphology. *Nat. Commun.* **2022**, *13* (3896), 1–12. <https://doi.org/10.1038/s41467-022-31507-w>.
- (18) Chen, X. R.; Yao, Y. X.; Yan, C.; Zhang, R.; Cheng, X. B.; Zhang, Q. A Diffusion--Reaction Competition Mechanism to Tailor Lithium Deposition for Lithium-Metal Batteries. *Angew. Chemie - Int. Ed.* **2020**, *59* (20), 7743–7747. <https://doi.org/10.1002/anie.202000375>.
- (19) Choudhury, S.; Huang, Z.; Amanchukwu, C. V.; Rudnicki, P. E.; Chen, Y.; Boyle, D. T.; Qin, J.; Cui, Y.; Bao, Z. Ion Conducting Polymer Interfaces for Lithium Metal Anodes : Impact on the

Electrodeposition Kinetics. *Adv. Energy Mater.* **2023**, *2301899*, 1–11.  
<https://doi.org/10.1002/aenm.202301899>.

- (20) Ren, X.; Zhang, Y.; Engelhard, M. H.; Li, Q.; Zhang, J. G.; Xu, W. Guided Lithium Metal Deposition and Improved Lithium Coulombic Efficiency through Synergistic Effects of LiAsF<sub>6</sub> and Cyclic Carbonate Additives. *ACS Energy Lett.* **2018**, *3* (1), 14–19.  
<https://doi.org/10.1021/acsenergylett.7b00982>.
- (21) Ren, X.; Zou, L.; Cao, X.; Engelhard, M. H.; Liu, W.; Burton, S. D.; Lee, H.; Niu, C.; Matthews, B. E.; Zhu, Z.; Wang, C.; Arey, B. W.; Xiao, J.; Liu, J.; Zhang, J. G.; Xu, W. Enabling High-Voltage Lithium-Metal Batteries under Practical Conditions. *Joule* **2019**, *3* (7), 1662–1676.  
<https://doi.org/10.1016/j.joule.2019.05.006>.
- (22) Oyakhire, S. T.; Liao, S. L.; Shuchi, S. B.; Kim, M. S.; Kim, S. C.; Yu, Z.; Vilá, R. A.; Rudnicki, P. E.; Cui, Y.; Bent, S. F. Proximity Matters: Interfacial Solvation Dictates Solid Electrolyte Interphase Composition. *Nano Lett.* **2023**, *23* (16), 7524–7531.  
<https://doi.org/10.1021/acs.nanolett.3c02037>.
- (23) Yoon, S. G.; Cavallaro, K. A.; Park, B. J.; Yook, H.; Han, J. W.; McDowell, M. T. Controlling Solvation and Solid-Electrolyte Interphase Formation to Enhance Lithium Interfacial Kinetics at Low Temperatures. *Adv. Funct. Mater.* **2023**. <https://doi.org/10.1002/adfm.202302778>.
- (24) Xie, J.; Sun, S.; Chen, X.; Hou, L.; Li, B.; Peng, H.; Huang, J.; Zhang, X.; Zhang, Q. Fluorinating the Solid Electrolyte Interphase by Rational Molecular Design for Practical Lithium-Metal Batteries. *Angew. Chemie* **2022**, *134* (29). <https://doi.org/10.1002/ange.202204776>.
- (25) Zhang, Z.; Li, Y.; Xu, R.; Zhou, W.; Li, Y.; Oyakhire, S. T.; Wu, Y.; Xu, J.; Wang, H.; Yu, Z.; Boyle, D. T.; Huang, W.; Ye, Y.; Chen, H.; Wan, J.; Bao, Z.; Chiu, W.; Cui, Y. Capturing the Swelling of Solid-Electrolyte Interphase in Lithium Metal Batteries. *Science (80-. ).* **2022**, *375* (6576), 66–70. <https://doi.org/10.1126/SCIENCE.ABI8703>.
- (26) Sayavong, P.; Zhang, W.; Oyakhire, S. T.; Boyle, D. T.; Chen, Y.; Kim, S. C.; Vilá, R. A.; Holmes, S. E.; Kim, M. S.; Bent, S. F.; Bao, Z.; Cui, Y. Dissolution of the Solid Electrolyte Interphase and Its Effects on Lithium Metal Anode Cyclability. *J. Am. Chem. Soc.* **2023**.  
<https://doi.org/10.1021/jacs.3c03195>.
- (27) Kim, S. C.; Oyakhire, S. T.; Athanitis, C.; Wang, J.; Zhang, Z.; Zhang, W.; Boyle, D. T.; Kim, M. S.; Yu, Z.; Gao, X.; Sogade, T.; Wu, E.; Qin, J.; Bao, Z.; Bent, S. F.; Cui, Y. Data-Driven Electrolyte Design for Lithium Metal Anodes. *Proc. Natl. Acad. Sci. U. S. A.* **2023**, *120* (10), e2214357120.  
<https://doi.org/10.1073/pnas.2214357120>.
- (28) Sendek, A. D.; Cubuk, E. D.; Antoniuk, E. R.; Cheon, G.; Cui, Y.; Reed, E. J. Machine Learning-Assisted Discovery of Solid Li-Ion Conducting Materials. *Chem. Mater.* **2019**, *31* (2), 342–352.  
<https://doi.org/10.1021/acs.chemmater.8b03272>.
- (29) Hastie, T.; Tibshirani, R.; James, G.; Witten, D. An Introduction to Statistical Learning (2nd Ed.). *Springer texts* **2021**, *102*, 618.
- (30) Sendek, A. D.; Ransom, B.; Cubuk, E. D.; Pellouchoud, L. A.; Nanda, J.; Reed, E. J. Machine Learning Modeling for Accelerated Battery Materials Design in the Small Data Regime. *Adv. Energy Mater.* **2022**, *12* (31), 1–20. <https://doi.org/10.1002/aenm.202200553>.
- (31) Oyakhire, S. T.; Gong, H.; Cui, Y.; Bao, Z.; Bent, S. F. An X-Ray Photoelectron Spectroscopy Primer for Solid Electrolyte Interphase Characterization in Lithium Metal Anodes. *ACS*

*Energy Lett.* **2022**, *7* (8), 2540–2546. <https://doi.org/10.1021/acsenergylett.2c01227>.

- (32) Lu, B.; Li, W.; Cheng, D.; Bhamwala, B.; Ceja, M.; Bao, W.; Fang, C.; Meng, Y. S. Suppressing Chemical Corrosions of Lithium Metal Anodes. *Adv. Energy Mater.* **2022**, *12* (48), 1–9. <https://doi.org/10.1002/aenm.202202012>.
- (33) Boyle, D. T.; Huang, W.; Wang, H.; Li, Y.; Chen, H.; Yu, Z.; Zhang, W.; Bao, Z.; Cui, Y. Corrosion of Lithium Metal Anodes during Calendar Ageing and Its Microscopic Origins. *Nat. Energy* **2021**, *6* (5), 487–494. <https://doi.org/10.1038/s41560-021-00787-9>.
- (34) Pei, A.; Zheng, G.; Shi, F.; Li, Y.; Cui, Y. Nanoscale Nucleation and Growth of Electrodeposited Lithium Metal. *Nano Lett.* **2017**, *17* (2), 1132–1139. <https://doi.org/10.1021/acs.nanolett.6b04755>.
- (35) Wasalathanthri, R. N.; Akolkar, R. Perspective—Does the Sand Equation Reliably Predict the Onset of Morphological Evolution in Lithium Electrodeposition? *J. Electrochem. Soc.* **2022**, *169* (9), 092519. <https://doi.org/10.1149/1945-7111/ac8d73>.
- (36) de Winter, J. C. F.; Gosling, S. D.; Potter, J. Comparing the Pearson and Spearman Correlation Coefficients across Distributions and Sample Sizes: A Tutorial Using Simulations and Empirical Data. *Psychol. Methods* **2016**, *21* (3), 273–290. <https://doi.org/10.1037/met0000079>.
- (37) Ding, J. F.; Xu, R.; Xiao, Y.; Zhang, S.; Song, T. L.; Yan, C.; Huang, J. Q. Dynamic Galvanic Corrosion of Working Lithium Metal Anode Under Practical Conditions. *Adv. Energy Mater.* **2023**, *13* (21), 1–8. <https://doi.org/10.1002/aenm.202204305>.
- (38) Lin, D.; Liu, Y.; Li, Y. Y.; Li, Y. Y.; Pei, A.; Xie, J.; Huang, W.; Cui, Y. Fast Galvanic Lithium Corrosion Involving a Kirkendall-Type Mechanism. *Nat. Chem.* **2019**, *11* (4), 382–389. <https://doi.org/10.1038/s41557-018-0203-8>.